

# Synthesis, Characterization, Optical and Transport Properties of BaSnO<sub>3</sub> Synthesized by Wet Chemical Route

Rakesh Kurre, Sharmila Bajpai, Parmendra Kumar Bajpai\*

Department of Pure & Applied Physics, Guru Ghasidas Vishwavidyalaya, Bilaspur, India

Email: \*bajpai.pk1@gmail.com

**How to cite this paper:** Kurre, R., Bajpai, S. and Bajpai, P.K. (2018) Synthesis, Characterization, Optical and Transport Properties of BaSnO<sub>3</sub> Synthesized by Wet Chemical Route. *Materials Sciences and Applications*, 9, 92-110.

<https://doi.org/10.4236/msa.2018.91007>

**Received:** September 7, 2017

**Accepted:** January 9, 2018

**Published:** January 12, 2018

Copyright © 2018 by authors and Scientific Research Publishing Inc. This work is licensed under the Creative Commons Attribution International License (CC BY 4.0).

<http://creativecommons.org/licenses/by/4.0/>



Open Access

## Abstract

Alkaline earth stannates have renewed attention as potential materials for gas sensing, transparent conducting oxides and ceramic capacitor applications. A noble wet chemical route is chosen to synthesize BaSnO<sub>3</sub> powders having micron size grains. Problems related to uneven grains and poor densification in conventional solid state route have been overcome in the present method. X-ray diffraction data confirms the single phase formation without any secondary phase having cubic perovskite structure (S.G. Pm-3 m). The estimated lattice parameter is  $\approx 4.11933 \text{ \AA}$  and percentage density is  $\approx 90\%$ . The microstructure probed by scanning electron micrograph reveals almost homogeneously distributed particles having random shape with some porosity. Phonon modes in FT-IR and Raman spectra confirm the local symmetry distortion. The DC conductivity at 200°C approaches almost  $2 \times 10^{-2} (\Omega\text{-cm})^{-1}$ , which is almost of the same order as that observed in perovskite based electronic conductors. DC and a.c. electrical conductivity of the material follow Mott's variable range hopping at low temperature and Arrhenius type thermally activated process at elevated temperatures. Evidence of small polaron formation is also verified. Optical band gap estimated from absorption data is  $\approx 2.94$  very close to the reported value. Composition prepared through the noble wet chemical route has high electrical conduction and suitable for gas sensing applications.

## Keywords

X-Ray Diffraction, Raman Spectra, Variable Range Hopping, Phonons

## 1. Introduction

Barium stannate (BaSnO<sub>3</sub>) belongs to the family of alkaline earth stannates hav-

ing the general chemical formula  $M\text{SnO}_3$  ( $M = \text{Ca, Ba, Sr}$ ) and has been studied widely due to their potential applications in the field of thermally stable capacitors, photo catalyst, chemiresistive sensor materials for toxic and noxious gases [1]-[6]. It stabilizes in cubic perovskite structure at room temperature (space group  $\text{Pm-3 m}$ ) with lattice parameter slightly varying from 0.4117 - 0.4119 nm depending upon the method of synthesis used [7] [8] [9] [10], and behaves like n-type semiconductor with an optical band gap reported from 3.1 - 3.4 eV [11] [12] [13] [14].  $\text{BaSnO}_3$  (BSO) compositions have been widely investigated with a view to improving the sensor response for a number of target gases including  $\text{NH}_3$ , Co,  $\text{H}_2$ ,  $\text{Cl}_2$ , LPG, ethanol,  $\text{NO}_x$ , humidity,  $\text{O}_2$ , etc. [15]-[20].

It may be noted that the bulk and surface electrical properties in polycrystalline ceramics are correlated with microstructure, grain size, density and intrinsic defects present in the material. For the synthesis of BSO powder, different physical and chemical methods are therefore, used to improve the conduction behavior. The solid state reaction route adopted mainly to improve the densification [21]-[26] encountered the problem of low densification and uneven grain growth. In solid state route, sintering in the range of  $1200^\circ\text{C}$  -  $1400^\circ\text{C}$  was inadequate for proper grain growth, inter granular connectivity and adequate densification [19]. BSO ceramics sintered even up to  $1600^\circ\text{C}$  for 12 h even could not eliminate the porosity and only after sintering for 72 h, the relative density > 95% was achieved [23]. Another major problem using high temperature sintering has been that the sintered material resulted into large anion defects and further that the high temperature processing is not compatible with sensor technology [27]. Self-heat sustained method [28] has been suggested as an alternate, and homogeneous grains of cubical nature are obtained in this method at  $1325^\circ\text{C}$ , however, the non-uniformity of grain size has not been addressed [19]. Chemical methods including oxalate co-precipitation method [10] [15] [16], sol-gel [7] [29] [30] [31] [32], sol-gel based wet chemical method [33] [34], hydrothermal [35] [36] [37], molten salt synthesis [38], polymerized complex route [39] [40] [41] [42], etc. have been reported. Most of these reports have focused towards smaller grain size so as to increase the surface area to improve the surface adsorption process. Despite large number of efforts devoted on the synthesis, detailed analysis of transport properties and their correlation with processing parameters based on systematic characterization of material structure at atomic level has been missing. In this paper, we tried to fill that gap and present the structural, microstructural features of the material synthesized through simple wet chemical method and probed the local structural details through FTIR and Raman spectroscopy. Optical band gap and electrical conduction mechanism operating in different temperature ranges are also probed.

## 2. Experimental Technique

The modified wet chemical method is used to synthesize barium stannate powders. The highly pure starting materials  $\text{BaCl}_2$  (Aldrich, 99.5%),  $\text{SnCl}_4 \cdot 5\text{H}_2\text{O}$  (Sig-

ma, 99.5%), NaOH (BDH, 99%), were used as received. A starting solution was made by mixing 20.823 g of anhydrous barium chloride ( $\text{BaCl}_2$ ) and 35.051 g of stannic chloride ( $\text{SnCl}_4$ ) in 100 ml deionized doubled distilled water. During this process 4 g sodium hydroxide was added into the solution. The solution was aged for 24 h, a white precipitate was obtained in the lower surface of solution. After filtering, the product was repeatedly washed by distilled water to remove  $\text{Cl}^-$  ions. The white powder was dried at  $80^\circ\text{C}$  for 24 h by using a muffle furnace. Finally, the dried barium stannate powders were annealed at  $800^\circ\text{C}$  in ambient environment.

Annealed powders were structurally analyzed using X-ray diffraction data which were measured on X-ray diffractometer (Rigaku Smart Lab, Japan). In order to make impedance measurements, the fine annealed powder was pressed as cylindrical pellets (diameter 10 - 12 mm and 1 - 2 mm thickness) after adding a few drops of poly vinyl alcohol (PVA) as binder. The prepared powder was again annealed at  $800^\circ\text{C}$  temperature in furnace for 5 h. After firing the samples were furnace cooled. The pellets were finally coated with conductive silver paint and dried at  $500^\circ\text{C}$  for 2 h before performing dielectric and impedance measurements.

The percentage porosity was calculated using measured experimental density (Archimedes principle as well as by measuring the weight, area and thickness of the pellet) and by calculating the theoretical density from XRD data. X-ray diffraction (XRD) studies of the materials were made at room temperature in the Bragg angle range  $20^\circ\text{C} \leq 2\theta \leq 80^\circ\text{C}$  with  $\text{CuK}\alpha$  radiation ( $\lambda = 1.5418 \text{ \AA}$ ) using  $\text{CuK}\beta$  filter. The complex impedance measurements over temperature range from  $35^\circ\text{C} - 300^\circ\text{C}$  were performed using a computer controlled impedance analyzer (HIOKI LCR Hi-TESTER MODEL 3532-50) in the frequency range 1 kHz to 1 MHz. Scanning electron microscopy (SEM) is used for the analysis of surface microstructure along with EDAX spectra. DC conductivity was measured by (Keithley) 6514 system electrometer. Room temperature FT-IR and Raman spectra were measured using Shimadzu 7800 FTIR and Technos micro Raman spectrometer respectively.

### 3. Result and Results and Discussion

#### 3.1. Structural Analysis

**Figure 1** shows the room temperature X-ray diffraction pattern of  $\text{BaSnO}_3$  powder prepared by wet chemical method. The XRD pattern shows peaks due to cubic perovskite structure only without any impurity peak. We have performed the Reitveld refinement on structural data using PDXL software with pseudo-Voight band profile in order to get the reliable estimate of the cubic cell parameters. **Table 1** presents the Lattice parameter, unit cell volume and goodness of fitting using Reitveld refinement technique. Accordingly, the value of cell parameter obtained is  $4.11933 \text{ \AA}$  which is very close to the literature value and the fitting parameters are also quite satisfactory. The fitting matches very well with

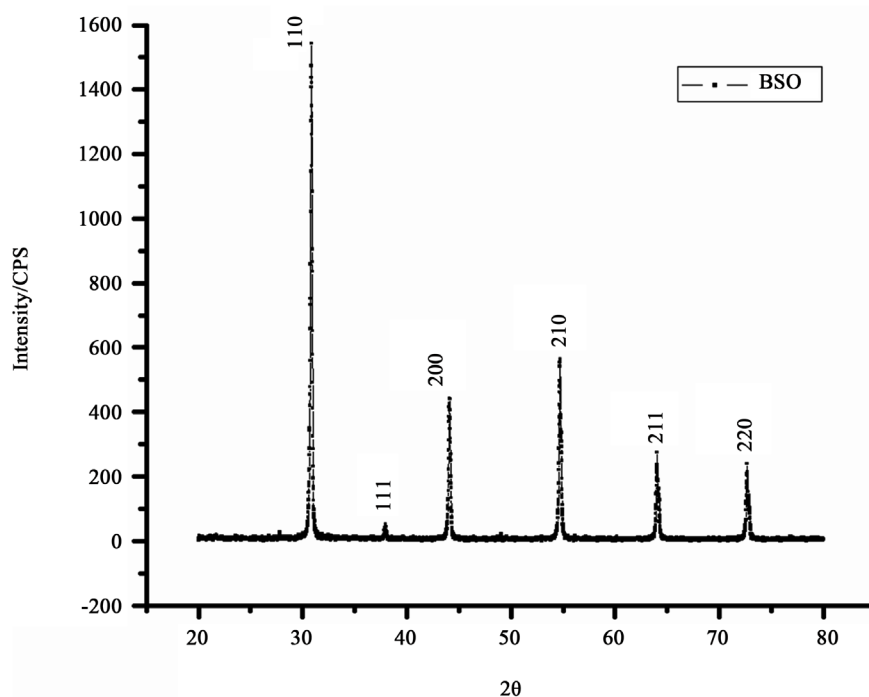


**Figure 1.** X-ray diffraction pattern of BSN powder prepared by wet chemical method.

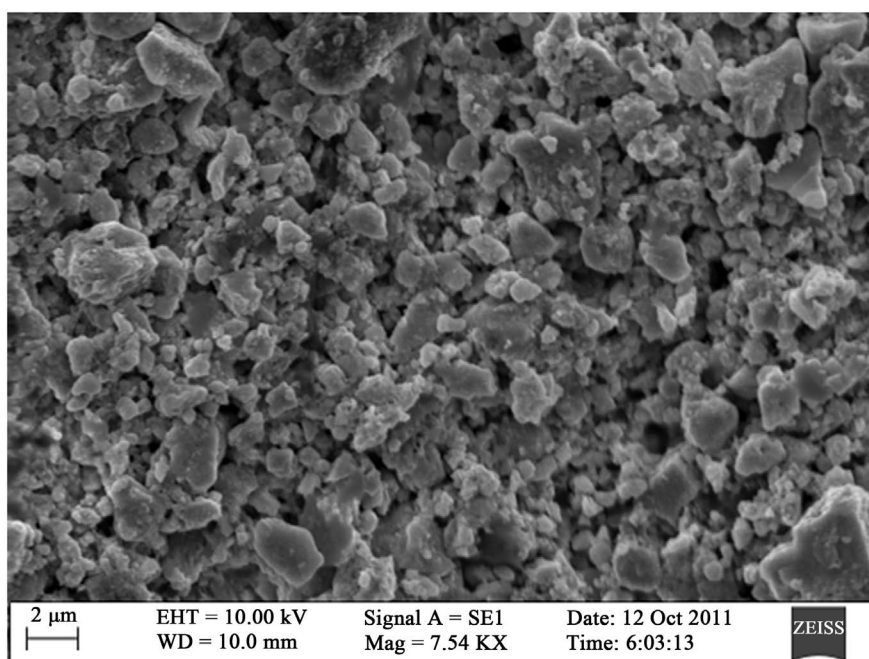
**Table 1.** Lattice parameter, unit cell volume and goodness of fitting using Reitveld refinement technique.

Pure BaSnO <sub>3</sub>					
a = 4.11933 (18) Å, V = 69.90 (5) Å <sup>3</sup> , Rp = 20.4, Chi <sup>2</sup> = 1.4235					
2θ	d-values	Intensity	Indices		
30.859	2.8953 (2)	348 (3)	h	k	l
37.964	2.3682 (10)	8.8 (5)	1	1	0
44.094	2.0521 (18)	114.3 (12)	1	1	1
54.703	1.6765 (12)	120 (8)	2	0	0
64.025	1.4531 (14)	51 (6)	2	0	0
72.661	1.3002 (11)	48 (4)	2	1	0

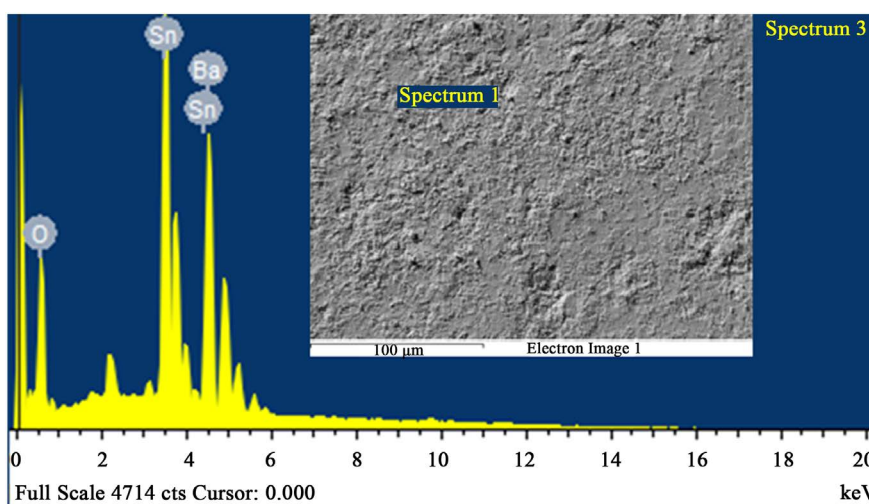
ICDD DB card No. 04-007-8719 and observed d-values shown in the table are also very close to the reference data. The formation of single phase material is confirmed as no extra XRD lines due to precursor oxides or minor secondary phases are traceable within the detection limit. The theoretical density of the unit cell was calculated from XRD data and density of the pellets was measured using Archimedes technique. Accordingly, the densification of ceramics is 91.7%. We also obtained the percentage density by simply weighing the pellets and measuring its volume which also comes out to be around 90%. The average crystallite size calculated using Scherrer method is ~42 nm. Small crystallite size may be the reason while higher densification is observed at relatively lower temperature.

### 3.2. Microstructural Characterization

The surface morphology was studied by scanning electron microscopy (Zeiss, EVO® MA 10). The surface microstructure is an important factor that controls the electrical properties through inter-grain connectivity. The SEM micrographs of the BSO powder synthesized by wet chemical route are shown in **Figure 2(a)**. Random grain growth is clearly visible with agglomeration of smaller particles forming the grains. Average grains size is estimated from linear intercept method using five different lines on the micrographs each having roughly 15 grains.



(a)



(b)

**Figure 2.** (a) Scanning electron microscope (SEM) micrograph of BaSnO<sub>3</sub> powder; (b) EDAX signal from section of BaSnO<sub>3</sub> surface. Inset shows the region from which the signal spectra are recorded.

The average grain size is  $\approx 2 \mu\text{m}$  with loosely interconnected grains. The average grain size in the sintered pellets remains same with homogeneous grain distribution. The elemental analysis and the chemical uniformity over the surface have been probed using EDAX spectra. The representative EDAX spectra are shown in **Figure 2(b)** from a section. Similar EDAX signals have been studied from various selected region over the surface. Elemental percentage in  $\text{BaSnO}_3$  sample are estimated from EDAX using standards  $\text{SiO}_2$  for O; Sn for Sn and  $\text{BaF}_2$  for Ba as shown in **Table 2**. The estimated values of Ba, Sn and oxygen atoms are very close to the stoichiometric composition. There is no significant difference in the elemental percentage obtained from different regions.

### 3.3. Nature of Phonon Modes

Raman spectroscopic studies of cubic perovskites have been extensively reported and spectral features are understood quite well [43] [44] [45] [46]. In the cubic phase (space group  $\text{Pm}\bar{3}\text{m}$ ), group theoretical analysis allows 12 optical modes ( $3\text{F}_{1\text{u}}$  and  $1\text{F}_{2\text{u}}$ ) that are Raman forbidden. Despite the fact that there are no allowed phonons in cubic perovskite phase, reported Raman spectra of BSO show a number of peaks coming from the first order Raman activity [47]. There are contradictory interpretations regarding the origin of these peaks [47] [48]. Recently, we have made an attempt to resolve the controversy and attributed the observed Raman activity due to local structural symmetry change induced by defects in the system [49]. This results into folding of  $\Gamma$ -point of Brillion zone (Zone Centre) into M- and or R-point (zone boundary), as suggested by DFT based calculations also [47]. Thus, Raman spectroscopy could be used to track the local structural changes occurring in the material during processing as first order Raman activity is forbidden in cubic phase. On the other hand, three optical phonons are active in IR viz.  $\text{TO}_1$ ,  $\text{TO}_2$  and  $\text{TO}_3$ ; the LO-TO splitting is expected due to ionic character of bonds.

The unpolarised room temperature Raman spectrum for the composition is shown in **Figure 3**. Raman modes due to BSO are observed at 135 and 241  $\text{cm}^{-1}$ . The band appearing at 152  $\text{cm}^{-1}$  is probably due to  $\text{BaCO}_3$  which may be formed if defects are present as reported earlier [50]. Non-observance of higher frequency modes in compositions is due to large background scattering suppressing these modes probably due to the presence of moisture. Appearance of modes

**Table 2.** Elemental percentage in  $\text{BaSnO}_3$  sample as estimated from EDAX using standards. Processing options: All elements analyzed (normalized), Number of iterations = 5. Standard: O  $\text{SiO}_2$ ; Sn Sn; Ba  $\text{BaF}_2$ .

Element	Weight %	Atomic %
O K	21.49	68.68
Sn L	35.95	15.48
Ba L	42.56	15.84
Totals	100.00	

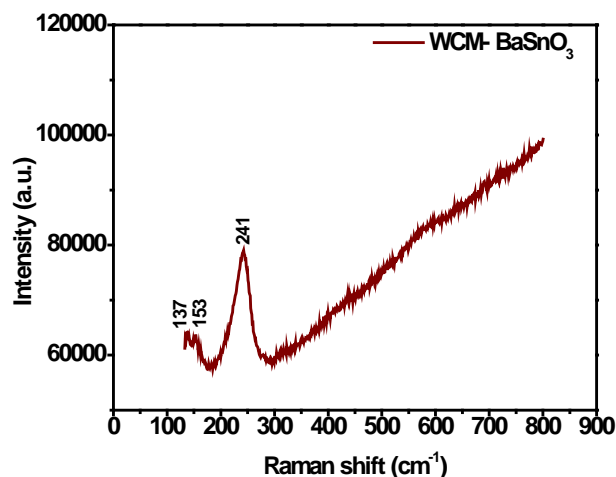


**Figure 3.** Room temperature unpolarised Raman spectrum of BSO powder prepared through wet chemical route.

at 135 and 241  $\text{cm}^{-1}$  assigned to BSO means the local symmetry structure is distorted from cubic symmetry.

The room temperature FTIR spectrum of BSO composition in the range 500  $\text{cm}^{-1}$  to 4000  $\text{cm}^{-1}$  is shown in **Figure 4**. The observed bands are also marked in the figure. The broad band appearing in the O-H stretching range (3000 - 3500  $\text{cm}^{-1}$ ) as well as those coming from ambient gases (1700 - 2300  $\text{cm}^{-1}$ ) appears clearly reflecting the presence of moisture in the composition. This may be due to porous nature of sample. The transverse optical modes of BSO in IR appears at 135, 244 and 668  $\text{cm}^{-1}$ , whereas corresponding longitudinal phonons are expected at 154, 421 and 723  $\text{cm}^{-1}$  as reported from IR reflectivity data [47]. Based on this, the strong band appearing at 668  $\text{cm}^{-1}$  could be assigned to BSO TO mode. The low frequency modes could not be observed due to experimental limitations in our experiment. Two bands appearing at 865 and 1446  $\text{cm}^{-1}$  could be associated with  $\text{BaCO}_3$  vibrational modes [51] and indicate the presence of small amount of  $\text{BaCO}_3$  in the samples below the detection limit of XRD. A shoulder around 421  $\text{cm}^{-1}$  is also visible in compositions assigned to LO mode clearly indicating that the LO-TO splitting is present and local structure is distorted from cubic symmetry as evident from Raman spectra also.

### 3.4. Optical Properties

The optical (UV-Vis) absorption spectrum for the BSO powder has been measured using Shimadzu UV 1700 Pharma spec spectrophotometer in the absorption mode. The spectrum is shown in **Figure 5**. Strong absorption bands around 250 nm and 430 nm are mainly due to optical transitions from valence band to conduction band involving  $\text{O}^{2-}$ : 2p and  $\text{Sn}^{4+}$ : 5s orbitals. An absorption tail towards NIR region is also observed. Theoretically, for direct band semiconductors, the absorption coefficient follows the relation [52]

$$\alpha(h\nu) \propto \sqrt{h\nu - E_g} / h\nu \quad (1)$$

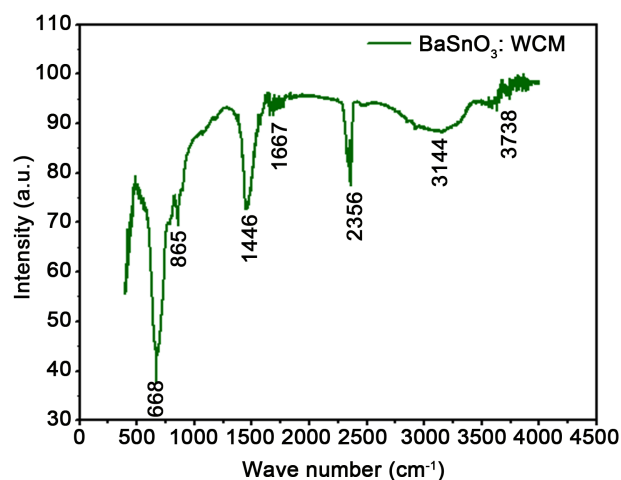


**Figure 4.** Room temperature FTIR spectrum of BSO powder prepared through wet chemical route.

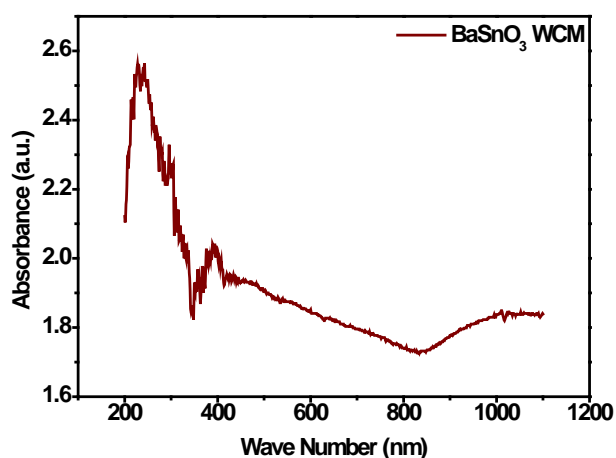


**Figure 5.** Optical absorption spectrum of BSO powder prepared through wet chemical route.

This leads to the Tauc relation given as

$$(\alpha h\nu)^2 = A(h\nu - E_g) \quad (2)$$

Here  $\alpha$  is the absorption coefficient,  $h\nu$  is the photon energy,  $A$  is a constant. Thus, the optical band gap energy ( $E_g$ ) can be calculated by plotting the graph between  $(\alpha h\nu)^2$  vs.  $(h\nu)$ . Band gap ( $E_g$ ) can be obtained by extrapolating the linear portion of the plot to the x axis, where  $(\alpha h\nu)^2 = 0$ . The Tauc plot is shown in **Figure 6(a)**. The calculated band gap energy is 2.85 eV, which is albeit smaller to those reported earlier [53]. The smaller value of optical band gap in comparison to the known band gap of  $\approx 3.1$  eV may be due to local states formation near the band edge. It is well known that band gap measurements using the Tauc plot require the precise determination of absorption coefficient ( $\alpha$ ) in order to get correct value of band gap. However, for this, it is necessary to perform corrections to the absorption due to reflection. We have therefore, used an alternate procedure called absorption spectra fitting (ASF) to calculate the band gap [54].

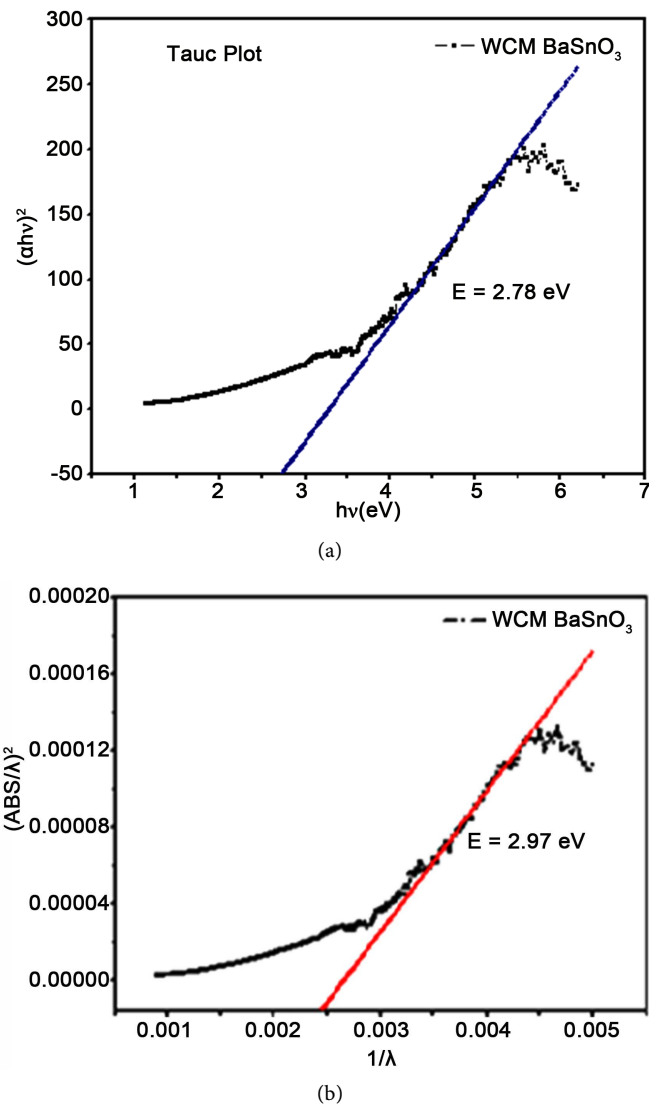


**Figure 6.** (a) Plot of  $(\alpha h\nu)^2$  vs.  $h\nu$  (Tauc plot (left) and (b)  $(\text{absorption}/\lambda)^2$  vs.  $1/\lambda$  plot used for calculating the optical band gap of BSO powder prepared by wet chemical route. The estimated band gaps are shown in the figures.

The absorption spectra fitting procedure (ASF) has advantage over Tauc plot method as the optical band gap can be determined directly from absorbance data and without having the need to measure the thickness of the sample and is not affected by local states due to disorder.

ASF procedure has been a simple modification of Tauc plot method. This could be done by rewriting Equation (1) as  $\alpha(\lambda) = A(hc)^{m-1} \lambda \left[ \frac{1}{\lambda} - \frac{1}{\lambda_g} \right]^m$ , and substituting  $\alpha(\lambda) = \frac{2.303 \times Abs(\lambda)}{d}$  using Beer's Lambert law gives

$$Abs(\lambda) = A_1 \lambda \left[ \frac{1}{\lambda} - \frac{1}{\lambda_g} \right]^m + A_2 \quad (3)$$

where  $A_1$  and  $A_2$  being constants. The value of parameter  $\lambda_g$  can be obtained by extrapolating the  $\left(\frac{Abs}{\lambda}\right)^{\frac{1}{m}}$  vs.  $\frac{1}{\lambda}$  plot linearly at  $\left(\frac{Abs}{\lambda}\right)^{\frac{1}{m}} = 0$ . The optical band gap energy ( $E_g$  in electron volt), can be calculated as  $E_g = \frac{1239.83}{\lambda_g}$ . The least square fitting of the absorption data has best fitting for  $m = 1/2$ . The plot  $\left(\frac{Abs}{\lambda}\right)^{\frac{1}{m}}$  vs.  $\frac{1}{\lambda}$  is shown in **Figure 6(b)**. The value of  $E_g$  (2.97 eV) is quite close to the reported values ranging from 3.1 - 3.4 eV.

### 3.5. Electrical Conductivity and Transport Properties

**Figure 7** shows the variation of d. c. electrical conductivity as a function of temperature. DC electrical conductivity increases with increase in temperature for all compositions showing typical semiconductor-like behavior. The observed value of dc electrical conductivity at room temperature is  $\approx 10^{-3} (\Omega \cdot \text{cm})^{-1}$  which increases and approaches  $10^{-2} (\Omega \cdot \text{cm})^{-1}$  at 200 °C. The observed high value of DC electrical conductivity approaching to those reported in perovskite electronic conductors [55].

DC electrical conductivity in n-type semiconductors is generally found to be thermally activated with Arrhenius form. The Arrhenius type plot ( $\log \sigma_{dc}$  Vs.  $1000/T$ ) (**Figure 7**) show non-linear variation and could be fitted into linear form in different temperature ranges with varying slope. This means that different thermally activated processes operative in different temperature ranges either involve different charge species or charge transport is being governed by hopping rather than being thermally activated. The activation energies are calculated using the relation  $\sigma = \sigma_0 \exp(-E_a/kT)$  where  $\sigma_0$ ,  $E_a$  and  $k$  are the pre-exponential factor, activation energy of the mobile charge carriers and

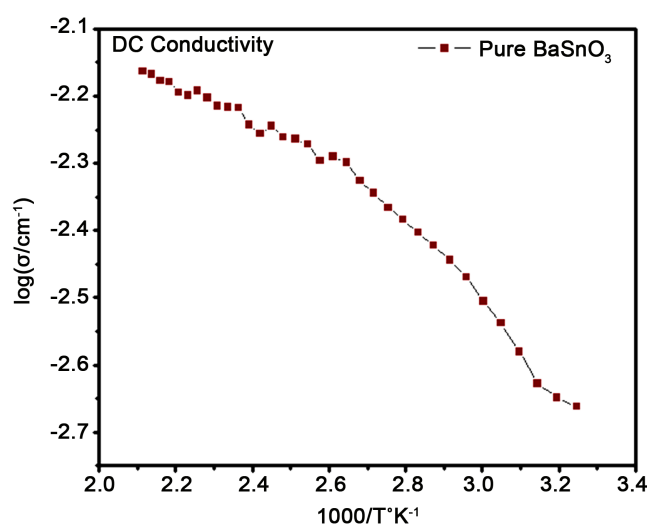


**Figure 7.** Arrhenius plot for dc electrical conductivity of BSO powder prepared by wet chemical method.

Boltzmann constant respectively. The calculated values of activation energies in different temperature ranges are shown in **Table 3**. The activation barrier energy varies significantly in different temperature range. It may be noted that the values of activation energies in the temperature range (35°C - 150°C), and (150°C - 200°C) are 0.08, and 0.44 eV respectively. This means different charge species are involved in the conduction process at low temperatures (35°C - 150°C) and high temperatures (150°C - 200°C). The typical values of activation energy at least in the lower temperature range are very small than the activation energy required for O<sup>2-</sup> vacancies (typically 0.5 eV) in the conduction process indicating that oxygen ion vacancies are not involved in dc conduction process up to 150°C.

It seems that low temperature conductivity mechanism may be Mott-type variable range hopping, whereas, at higher temperature, it may be thermally activated Arrhenius type. To get a clear picture of conductivity mechanism and to understand the transport behavior, the role of electronic structure of the doping becomes crucial [56]. However, in pure material, defects (intrinsic) generated during synthesis may modify Sn structure partially reducing Sn<sup>4+</sup> into Sn<sup>2+</sup>, increasing charge carrier density and also creating disorder in the octahedral (SnO<sub>6</sub>) units restricting the long range motion of charge species. Thus, conduction may occur due to hopping of electron between equivalent sites. As per the Mott's variable range hopping (VRH) model, the electrical conductivity in bulk due to hopping can be expressed as [57]

$$\sigma(T) = \sigma_0 \exp\left(-\left(\frac{T_0}{T}\right)^{1/4}\right) \quad (4)$$

Here  $T_0$  is the Mott's characteristic temperature which depends on density of states in the vicinity of Fermi energy and localization length "a" given as [58]

$$T_0 = \frac{18}{k_B N(E_F) a^3} \quad (5)$$

The mean hopping distance  $R_h(T)$  and hopping energy  $E_h(T)$  at a given temperature  $T$  could also be estimated in terms of  $T_0$  and localization length as given by [59]

**Table 3.** Calculated activation energies in different temperature ranges using Arrhenius relation.

Sample variation in kHz	Temperature range		
	Activation energy in eV (50°C - 85°C)	Activation energy in eV (90°C - 235°C)	Activation energy in eV (240°C - 300°C)
1 kHz	0.408	0.141	0.833
10 kHz	0.442	0.144	0.719
50 kHz	0.283	0.735	0.590
100 kHz	0.228	0.491	0.548
1000 kHz	0.114	0.394	0.375

$$R_h(T) = \frac{3}{8} a \left( \frac{T_0}{T} \right)^{1/4} \quad (6)$$

And

$$E_h(T) = \frac{1}{4} k_B T^{3/4} T_0^{1/4} \quad (7)$$

We fitted the temperature dependent dc electrical conductivity data using Mott's VRH model (Equation (4)) as shown in **Figure 8(a)**. The plots reveal that the range of temperature in which data could be fitted with VRH model is restricted only at higher temperatures. This means that the conduction mechanism is dominantly governed by the disorder induced localization of charges at elevated temperatures.

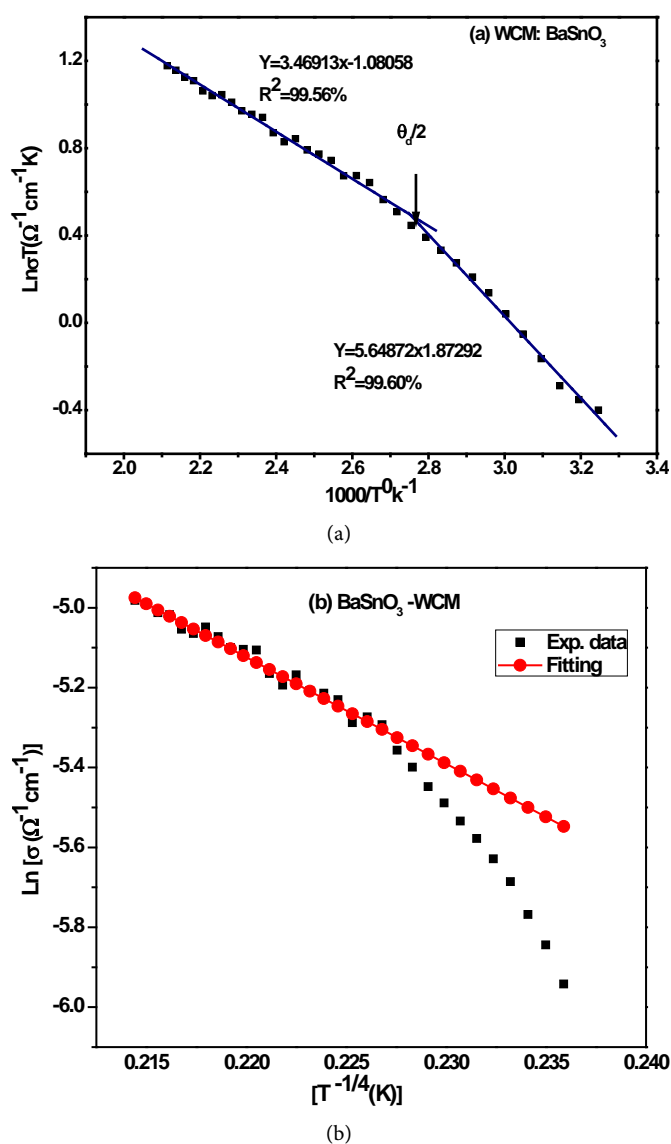


**Figure 8.** (a) Plot of temperature dependent DC conductivity data fitted with Mott-Davis small polaron approach. Lines are theoretical fit to Equation (7), and (b) theoretical fit using Mott's variable range hopping approach, Equation (1).

Some reports have also indicated the role of small polaron in the conduction in alkali earth stannates [60]. A small polaron may be formed when an excess of charge carriers moves slowly and stays at some atomic position so as to allow the coordinate ion to adjust its position due to the presence of the carrier. The conduction may take place by diffusion of electrons at localized sites. In fact, in La-substituted SrSnO<sub>3</sub>, it is suggested that conduction occurs through low polaron hopping of electrons between localized ions Sn<sup>4+</sup>/Sn<sup>2+</sup>.

In order to confirm the nature of hopping conduction, we use Mott-Davis small polaron hopping model [61] which has been found successful in many rare earth transition metal oxide systems at high temperature including Fe-substituted SrSnO<sub>3</sub> [62]. According to small polaron hopping, the temperature dependent electrical conductivity can be expressed as

$$\sigma T = \sigma_k \exp\left(\frac{E_p}{k_B T}\right) \quad (8)$$

where  $E_p$  is the activation energy,  $k_B$  is the Boltzmann constant and  $T$  is absolute temperature. In order to estimate the polaron hopping energy, we plotted the  $\ln(\sigma T)$  vs.  $1000/T$  in **Figure 8(b)**. The activation energy is related to polaron hopping energy ( $W_H$ ) and disorder energy ( $W_D$ ) in the temperature range given by [63]

$$E_p = \begin{cases} W_H + W_D/2 & (T > \theta_D/2) \\ W_D & (T < \theta_D/4) \end{cases} \quad (9)$$

Here  $\theta_D$  is Debye temperature. The plot( $\log \sigma T$  vs.  $1000/T$ ) deviates from straight line at certain value of temperature denoted by  $\theta_D/2$  in **Figure 8(b)**. The slope of high temperature side (above  $\theta_D/2$ ) has been used to estimate the activation energy of polaron ( $E_p$ ), which comes out to be 0.08 eV. Analysis clearly reveals that oxygen vacancies are not the dominant defects involved in charge transport and probably protonic type of conduction takes place with small polaron formation being evident at higher temperatures.

### 3.6. AC Conductivity

**Figure 9** shows the frequency variation of ac conductivity ( $\sigma_{ac}$ ) at different temperatures. The ac conductivity was calculated from the impedance data using the relation  $\sigma_{ac} = \omega \varepsilon_0 \varepsilon_r (\tan \delta)$ . The conductivity spectra at different temperatures show some typical behavior; no dispersion has been observed in the low frequency range of measurements with almost frequency independent low frequency plateau observed up to 250°C. However, a. c. conductivity shows significant increase at 300°C. Further, in the high frequency region dispersion is observed with the conductivity variation becoming non-linear at higher temperature. The frequency independent region shows a general trend; the region shifts towards higher frequency side with increase in temperature. These results indicate the existence of multiple relaxation processes and thermally activated charge species in the materials. The frequency at which change in slope of the of the

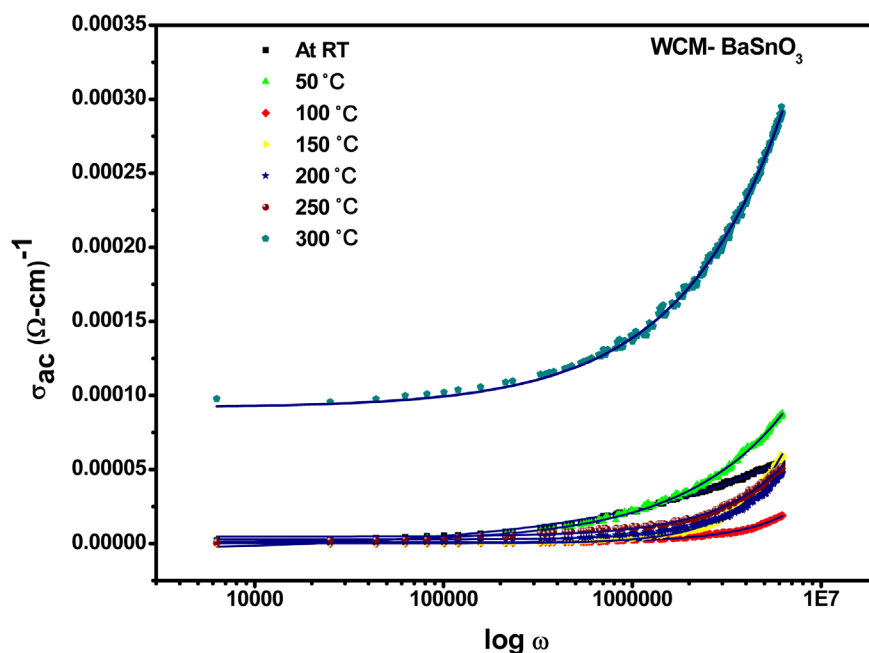


**Figure 9.** Frequency variation of a. c. electrical conductivity at representative temperatures (shown in figure). The lines in each plot are theoretical fit using Jonscher's universal power law (Equation (7) in the manuscript).

pattern occurs is known as hopping frequency ( $\omega_p$ ) suggesting that the electrical conduction occurs via hopping mechanism governed by Jonscher's power law [64].

The frequency dependence of a. c. conductivity may arise due to free as well as bound charge carriers. In case of conduction being due to free carriers the conductivity showed decrease with increase in frequency [65]. In our case, a. c. conductivity remains frequency independent and increases with frequency only after a certain frequency; therefore, bound charges trapped in the materials seems to be mainly responsible for conduction. Energy required for the relaxation/orientational process is lower than that required for mobility of charge carriers over a long distance. The observed almost frequency independent ac activation energy at lower frequencies indicates that contribution due to long range charge mobility is insignificant in the material.

The frequency dependence of conductivity is fitted with Jonscher's power law relation [64],

$$\sigma(\omega) = \sigma_{dc} + A\omega^n \quad (10)$$

where  $\sigma_{dc}$  is the frequency independent conductivity and the coefficient  $A$  and exponent  $n$  are temperature and material dependent. The term  $A\omega^n$  contains ac dependence and characterizes all dispersion phenomena. The exponent  $n$  show different dependence with temperature in different systems *i.e.* remains constant, decreasing with temperature, increasing with temperature but always varies between  $0 < n < 1$ . The variation of ac conductivity ( $\sigma_{ac}$ ) with frequency at different temperatures, along with the fitting with Jonscher's relation, is shown

in **Figure 9**. From the theoretical fit (lines in the plot) it is evident that ac electrical conductivity spectrum obeys Jonscher's power law at all frequencies; hence electrical conduction of the materials is thermally activated process at these frequencies. According to Jonscher [64], the origin of the frequency dependent conductivity lies in the motion of mobile charge carriers. When a mobile charge carrier hops to a new site from its original position, it remains in a state of displacement between two potential energy minima. After a sufficiently long time, the defect could relax until the two minima of lattice potential energy coincide with the lattice site.

#### 4. Conclusion

Phase pure  $\text{BaSnO}_3$  powder has been successfully synthesized using simple wet chemical route. Composition is stabilized in average cubic structure (Pm-3 m). Nature of the vibrational modes in both IR and Raman reveals local symmetry distortion probably due to intrinsic defects generated during synthesis. The optical band gap is 2.95 eV, very close to the reported value. The high value of dc electrical conductivity at room temperature, almost dispersion free and temperature independent nature of a. c. conductivity spectra reflect significant improvement in the electrical behavior of the composition with respect to those reported from conventional solid state route. The conduction mechanism is found to be governed by Mott's variable range hopping mechanism at lower temperature and thermally activated at elevated temperatures. Small polaron formation also seems to be the possibility at high temperature. Small values of activation energy derived from conductivity data rule out the possibility of oxygen vacancies being involved in dc conduction process.

#### Acknowledgements

PKB is thankful to Department of Science & Technology (DST), Govt. of India for providing support under FIST program and the University Grants Commission (UGC), New Delhi for the financial support under SAP program.

#### References

- [1] Moseley, P.T., Williams, D.E., Norris, J.O.W. and Tofield, B.C. (1988) Electrical Conductivity and Gas Sensitivity of Some Transition Metal Tantalates. *Sensors and Actuators*, **14**, 79-91. [https://doi.org/10.1016/0250-6874\(88\)80008-8](https://doi.org/10.1016/0250-6874(88)80008-8)
- [2] Shimizu, Y., Shimabukuro, M., Arai, H. and Seiyama, T. (1989) Humidity—Sensitive Characteristics of  $\text{La}^{3+}$ -Doped and Undoped  $\text{SrSnO}_3$ . *Journal of Electrochemical Society*, **136**, 1206. <https://doi.org/10.1149/1.2096854>
- [3] Lumpe, U., Gerblinger, J. and Meixner, H. (1995) Carbon-Monoxide Sensors Based on Thin Films of  $\text{BaSnO}_3$ . *Sensors and Actuators B*, **24-25**, 657-660. [https://doi.org/10.1016/0925-4005\(95\)85145-3](https://doi.org/10.1016/0925-4005(95)85145-3)
- [4] Lumpe, U., Gerblinger, J. and Meixner, H. (1995) Nitrogen Oxide Sensors Based on Thin Films of  $\text{BaSnO}_3$ . *Sensors and Actuators B*, **26-27**, 97-98. [https://doi.org/10.1016/0925-4005\(94\)01565-Y](https://doi.org/10.1016/0925-4005(94)01565-Y)
- [5] Kocemba, I., Jedrzejewska, M.W., Szychowska, A., Rynkowski, J. and Gowka, M.

- (2007) The Properties of Barium Stannate and Aluminum Oxide-Based Gas Sensor: The Role of  $\text{Al}_2\text{O}_3$  in This System. *Sensors and Actuators B*, **121**, 401-405. <https://doi.org/10.1016/j.snb.2006.03.052>
- [6] Bajpai, P.K., Ratre, K., Pastore, M. and Sinha, T.P. (2003) Preparation, Characterization and Dielectric Behaviour of Some Yttrium Doped Strontium Stannates. *Bulletin of Materials Science*, **26**, 461-464. <https://doi.org/10.1007/BF02707341>
- [7] Licheron, M., Jouan, G. and Husson, E. (1995) Characterization of  $\text{BaSnO}_3$  Powder Obtained by a Modified Sol-Gel Route. *Journal of the European Ceramic Society*, **17**, 1453-1457. [https://doi.org/10.1016/S0955-2219\(97\)00002-2](https://doi.org/10.1016/S0955-2219(97)00002-2)
- [8] Kutty, T.R.N. and Vivekanandan, R. (1987)  $\text{BaSnO}_3$  Fine Powders from Hydrothermal Preparations. *Materials Research Bulletin*, **22**, 1457-1465. [https://doi.org/10.1016/0025-5408\(87\)90210-8](https://doi.org/10.1016/0025-5408(87)90210-8)
- [9] Udawatte, C.P., Kakihana, M. and Yoshimura, M. (1998) Preparation of Pure Perovskite-Type  $\text{BaSnO}_3$  Powders by the Polymerized Complex Method at Reduced Temperature. *Solid State Ionics*, **108**, 23-30. [https://doi.org/10.1016/S0167-2738\(98\)00014-9](https://doi.org/10.1016/S0167-2738(98)00014-9)
- [10] Song, Y.J. and Kim, S. (2001) Preparation of Fine  $\text{BaSnO}_3$  Powders by Oxalate Coprecipitation Method. *Journal of Industrial and Engineering Chemistry*, **7**, 183-185.
- [11] Smith, A.J. and Welch, A.J. E. (1960) Some Mixed Metal Oxides of Perovskite Structure. *Acta Crystallographica*, **13**, 653-656. <https://doi.org/10.1107/S0365110X60001540>
- [12] Mountstevens, E.H., Attfeld, J.P. and Redfern, S.A.T. (2003) Cation-Size Control of Structural Phase Transitions in Tin Perovskites. *Journal of Physics: Condensed Matter*, **15**, 8315-8326. <https://doi.org/10.1088/0953-8984/15/49/010>
- [13] Larramona, G., Gutierrez, C., Pereira, I., Nunes, M.R. and Da Costa, F.M.A. (1989) Characterization of the Mixed Perovskite  $\text{BaSn}_{1-x}\text{Sb}_x\text{O}_3$  by Electrolyte Electroreflectance, Diffuse Reflectance, and X-Ray Photoelectron Spectroscopy. *Journal of the Chemical Society, Faraday Transactions 1*, **85**, 907-916. <https://doi.org/10.1039/f19898500907>
- [14] Mizoguchi, H., Woodward, P.M., Park, C.H. and Keszler, D.H. (2004) Strong Near-Infrared Luminescence in  $\text{BaSnO}_3$ . *Journal of American Chemical Society*, **126**, 9796-9800. <https://doi.org/10.1021/ja048866i>
- [15] Gopal Reddy, C.V., Manorama, S.V. and Rao, V. J. (2001) Preparation and Characterization of Barium Stannate: Application as a Liquefied Petroleum Gas Sensor. *Journal of Materials Science*, **12**, 137-142.
- [16] Tao, S., Gao, F., Liu, X. and Sorensen, O.T. (2000) Ethanol-Sensing Characteristics of Barium Stannate Prepared by Chemical Precipitation. *Sensors and Actuators B*, **71**, 223-227.
- [17] Cerda, J., Arbiol, J. and Dezanneau, G. (2002) Perovskite-Type  $\text{BaSnO}_3$  Powders for High Temperature Gas Sensor Applications. *Sensors and Actuators B*, **84**, 21-25. [https://doi.org/10.1016/S0925-4005\(02\)00005-9](https://doi.org/10.1016/S0925-4005(02)00005-9)
- [18] Jayaraman, V., Manhamma, G., Ganannasekaran, T. and Periaswami, G. (1996) Evaluation of  $\text{BaSnO}_3$  and  $\text{Ba}(\text{Zr},\text{Sn})\text{O}_3$  Solid Solutions as Semiconductor Sensor Materials. *Solid State Ionics*, **86-88**, 1111-1114. [https://doi.org/10.1016/0167-2738\(96\)00277-9](https://doi.org/10.1016/0167-2738(96)00277-9)
- [19] Doroftei, C., Popa, P.D. and Iacomi, F. (2012) Study of the Influence of Nickel Ions Substitutes in Barium Stannates Used as Humidity Resistive Sensors. *Sensors and Actuators A*, **173**, 24-29. <https://doi.org/10.1016/j.sna.2011.10.007>
- [20] Upadhyay, S. and Kavitha, P. (2007) Lanthanum Doped Barium Stannate for Hu-

- midity Sensor. *Materials Letters*, **61**, 1912-1915.  
<https://doi.org/10.1016/j.matlet.2006.07.154>
- [21] Upadhyay, S., Prakask, O. and Kumar, D. (1997) Preparation and Characterization of Barium Stannate BaSnO<sub>3</sub>. *Journal of Materials Science Letters*, **16**, 1330-1332.  
<https://doi.org/10.1023/A:1018559932473>
- [22] Farfan, J.C., Rodriguez, J.A., Fajardo, F., Vera Lopez, E., Tellez, D.A.L. and Rojas, J.R. (2009) structural Properties, Electric Response and Electronic Feature of BaSnO<sub>3</sub> Perovskite. *Physica B*, **404**, 2720-2722.  
<https://doi.org/10.1016/j.physb.2009.06.126>
- [23] Azad, A.M. and Hon, N.C. (1998) Characterization of BaSnO<sub>3</sub>-Based Ceramics: Part 1. Synthesis, Processing and Microstructural Development. *Journal of Alloys and Compounds*, **270**, 95-106. [https://doi.org/10.1016/S0925-8388\(98\)00370-3](https://doi.org/10.1016/S0925-8388(98)00370-3)
- [24] Smith, M.G., Goodenough, J.B., Manthiram, A., Taylor, R.D., Peng, W. and Kimball, C.W. (1992) Tin and Antimony Valence States in BaSn<sub>0.85</sub>Sb<sub>0.15</sub>O<sub>3-δ</sub>. *Journal of Solid State Chemistry*, **98**, 181. [https://doi.org/10.1016/0022-4596\(92\)90084-9](https://doi.org/10.1016/0022-4596(92)90084-9)
- [25] Bao, M., Lee, W.D. and Zhu, P. (1993) Dy on the Dielectric Properties of Oxide-Doped Ba(Ti,Sn)O<sub>3</sub> Ceramics Prepared from Ultrafine Powder. *Journal of Materials Science*, **28**, 6617. <https://doi.org/10.1007/BF00356405>
- [26] Upadhyay, S. (2013) High Temperature Impedance Spectroscopy of Barium Stannate, BaSnO<sub>3</sub>. *Bulletin of Materials Science*, **36**, 1019-1036.  
<https://doi.org/10.1007/s12034-013-0578-5>
- [27] Soni, P. and Bajpai, P.K. (2011) Synthesis and Dielectric Characterization of Non-Lead Based Perovskite Ceramics Ba<sub>1-x</sub>Sr<sub>x</sub>SnO<sub>3</sub>. *AIP Conference Proceedings*, **1372**, 184. <https://doi.org/10.1063/1.3644440>
- [28] Yi, H.C. and Moore, J.J. (1990) Self-Propagating High-Temperature (Combustion) Synthesis (SHS) of Powder-Compacted Materials. *Journal of Materials Science*, **25**, 1159. <https://doi.org/10.1007/BF00585421>
- [29] Creda, J., Arbil, J., Diaz, R., Dezannweau, G. and Morante, J.R. (2002) Synthesis of Perovskite-Type BaSnO<sub>3</sub> Particles Obtained by a New Simple Wet Chemical Route Based on a Sol-Gel Process. *Material Letters*, **56**, 131-136.  
[https://doi.org/10.1016/S0167-577X\(02\)00428-7](https://doi.org/10.1016/S0167-577X(02)00428-7)
- [30] Nakagauchi, R. and Kozuka, H. (2007) Preparation of Ba(Ti,Sn)O<sub>3</sub> Thin Films by PVP-Assisted Sol-Gel Method and Their Dielectric Properties. *Journal of Sol-Gel Science and Technology*, **42**, 221-229. <https://doi.org/10.1007/s10971-007-0772-2>
- [31] Azad, A.M., Hashim, M. and Baptist, S. (2000) Phase Evolution and Microstructural Development in Sol-Gel Derived MSnO<sub>3</sub> (M = Ca, Sr and Ba). *Journal of Materials Science*, **35**, 5475-5483. <https://doi.org/10.1023/A:1004825130403>
- [32] Song, S., Zhai, J., Gao, L. and Yao, X. (2009) Orientation-Dependent Dielectric Properties of Ba(Sn<sub>0.15</sub>Ti<sub>0.85</sub>)O<sub>3</sub> Thin Films Prepared by Sol-Gel Method. *Journal of Physics and Chemistry of Solids*, **70**, 1213-1217.  
<https://doi.org/10.1016/j.jpics.2009.07.007>
- [33] Lu, W. and Schmidt, H. (2007) Synthesis of Nanosized BaSnO<sub>3</sub> Powders from Metal Isopropoxides. *Journal of Sol-Gel Science and Technology*, **42**, 55-64.
- [34] Wang, Y., Chesnaud, A., Bevillon, E., Yang, J. and Dezanneau, G. (2011) Synthesis, Structure and Protonic Conduction of BaSn<sub>0.875</sub>M<sub>0.125</sub>O<sub>3-δ</sub> (M = Sc, Y, In and Gd). *International Journal of Hydrogen Energy*, **36**, 7688-7695.
- [35] Lu, W. and Schmidt, H. (2005) Hydrothermal Synthesis of Nanocrystalline BaSnO<sub>3</sub> Using a SnO<sub>2</sub>·xH<sub>2</sub>O Sol. *Journal of European Ceramic Society*, **25**, 919-925.

- <https://doi.org/10.1016/j.jeurceramsoc.2004.04.010>
- [36] Lu, W. and Schmidt, H. (2008) Lyothermal Synthesis of Nanocrystalline BaSnO<sub>3</sub> Powders. *Ceramic International*, **34**, 645-649. <https://doi.org/10.1016/j.ceramint.2007.01.002>
- [37] Patil, N.U. and Jain, G.H. (2012) Synthesis, Characterization and Performance of Pure and Surface Modified Nano-BaSnO<sub>3</sub> with TiO<sub>2</sub> Thick Film Resistor as a Gas Sensor. *Proceedings of 6th International Conference on Sensing Technology ICST*, Kolkata, 18-21 December 2012, 704-708.
- [38] Ramdas, B. and Vijayaraghavan, R. (2010) Low Temperature Synthesis of Ba<sub>1-x</sub>Sr<sub>x</sub>SnO<sub>3</sub> (x = 0 - 1) from Molten Alkali Hydroxide Flux. *Bulletin of Materials Science*, **33**, 75-78. <https://doi.org/10.1007/s12034-010-0011-2>
- [39] Yasukawa, M., Kono, T., Ueda, K., Yanagi, H. and Hosono, H. (2009) High-Temperature Thermoelectric Properties of La-Doped BaSnO<sub>3</sub> Ceramics. *Materials Science and Engineering B*, **173**, 29-32. <https://doi.org/10.1016/j.mseb.2009.10.002>
- [40] Bevillon, E., Chesnaud, A., Wang, Y., Dezanneau, G. and Geneste, G. (2008) Theoretical and Experimental Study of the Structural, Dynamical and Dielectric Properties of Perovskite BaSnO<sub>3</sub>. *Journal of Physics: Condensed Matter*, **20**, 145217-145222. <https://doi.org/10.1088/0953-8984/20/14/145217>
- [41] Köferstein, R., Jäger, L., Zenkner, M. and Ebbinghaus, S.G. (2009) Nano-Sized BaSnO<sub>3</sub> Powder via a Precursor Route: Comparative Study of Sintering Behaviour and Mechanism of Fine and Coarse-Grained Powders. *Journal of European Ceramic Society*, **29**, 2317-2324. <https://doi.org/10.1016/j.jeurceramsoc.2009.01.026>
- [42] Alves, M.C.F., Souza, S.C., Lima, H.H.S. and Nascimento, M.R. (2009) Influence of the Modifier on the Short and Long Range Disorder of Stannate Perovskites. *Journal of Alloys and Compounds*, **476**, 507-512. <https://doi.org/10.1016/j.jallcom.2008.09.034>
- [43] Jiang, Y.J., Zeng, L.Z., Wang, R.P., Zhu, Y. and Liu, Y.L. (1996) Fundamental and Second-Order Raman Spectra of BaTiO<sub>3</sub>. *Journal of Raman Spectroscopy*, **27**, 31-34. [https://doi.org/10.1002/\(SICI\)1097-4555\(199601\)27:1<31::AID-JRS920>3.0.CO;2-K](https://doi.org/10.1002/(SICI)1097-4555(199601)27:1<31::AID-JRS920>3.0.CO;2-K)
- [44] Naik, R., Nazarko, J.J., Flattery, C.S., Venkateswaran, U.D., Naik, V.M., Mohammed, M.S., Auner, G.W., Mantese, J.V., Schubring, N.W., Micheli, A.L. and Catalan, A.B. (2000) Temperature Dependence of the Raman Spectra of Polycrystalline Ba<sub>1-x</sub>SixTiO<sub>3</sub>. *Physical Review B*, **61**, 11367.
- [45] Begg, B.D., Finnie, K.S. and Vance, E.R. (1996) Raman Study of the Relationship between Room-Temperature Tetragonality and the Curie Point of Barium Titanate. *Journal of the American Ceramic Society*, **79**, 2666-2672. <https://doi.org/10.1111/j.1151-2916.1996.tb09032.x>
- [46] Kamba, S., Samoukhina, P., Kadlec, F., Pokorny, J. and Reaney, I.M. (2003) Composition Dependence of the Lattice Vibrations in Sr<sub>n+1</sub>Ti<sub>n</sub>O<sub>3n+1</sub> Ruddlesden-Popper Homologous Series. *Journal of the European Ceramic Society*, **23**, 2639-2645. [https://doi.org/10.1016/S0955-2219\(03\)00150-X](https://doi.org/10.1016/S0955-2219(03)00150-X)
- [47] Stanislavchuk, T.N., Sirenko, A.A., Litvinchuk, A.P., Luo, X. and Cheong, S.-W. (2012) Electronic Band Structure and Optical Phonons of BaSnO<sub>3</sub> and Ba<sub>0.97</sub>La<sub>0.03</sub>SnO<sub>3</sub> Single Crystals: Theory and Experiment. *Journal of Applied Physics*, **112**, Article ID: 044108. <https://doi.org/10.1063/1.4748309>
- [48] Abrashev, M.V., Backstrom, J., Borjesson, L., Popov, V.N., Chakalov, R.A., Kolev, N., Meng, R.-L. and Iliev, M.N. (2002) Raman Spectroscopy of CaMnO<sub>3</sub>: Mode Assignment and Relationship between Raman Line Intensities and Structural Distortions. *Physical Review B*, **65**, Article ID: 184301.

- <https://doi.org/10.1103/PhysRevB.65.184301>
- [49] Bajpai, S. and Bajpai, P.K. (2017) Defect Structure in Charge Compensated Lanthanum Doped BaSnO<sub>3</sub> as Probed by Raman Spectroscopy.
- [50] Tarari, M., Daumerc, J.P., Dordor, P., Pouchard, M., Behr, G. and Krabbes, G. (1994) Preparation and Characterization of Lanthanum Doped BaSnO<sub>3</sub>, *Journal of Physics and Chemistry of Solids*, **55**, 1239-1243. [https://doi.org/10.1016/0022-3697\(94\)90205-4](https://doi.org/10.1016/0022-3697(94)90205-4)
- [51] Nakamoto, K. (2008) Infrared Spectra of Inorganic and Coordination Compounds. 6th Edition, Wiley Publications, Hoboken.
- [52] Tauc, J. (1968) Optical Properties and Electronic Structure of Amorphous Ge and Si. *Materials Research Bulletin*, **3**, 37-46. [https://doi.org/10.1016/0025-5408\(68\)90023-8](https://doi.org/10.1016/0025-5408(68)90023-8)
- [53] Mizoguchi, H., Chen, P., Boolehand, P., Kuenofotov, V., Felser, G., Barnes, P.W. and Woodward, P.M. (2013) Electrical and Optical Properties of Sb-Doped BaSnO<sub>3</sub>. *Chemistry of Materials*, **25**, 3858-3866. <https://doi.org/10.1021/cm4019309>
- [54] Gobadi, N. (2013) Band Gap Determination using Absorption Spectrum Fitting Procedure. *International Nano Letters*, **3**, 2. <https://doi.org/10.1186/2228-5326-3-2>
- [55] Li, M., Pietrowski, M.J., De Souza, R.A., Zhang, H., Reaney, I.M., Cook, S.N., Kilner, J.A. and Sinclair, D.C. (2014) A Family of Oxide Ion Conductors Based on the Ferroelectric Perovskite Na<sub>0.5</sub>Bi<sub>0.5</sub>TiO<sub>3</sub>. *Nature Materials*, **13**, 31-35. <https://doi.org/10.1038/nmat3782>
- [56] Salssi, A. (2015) Ab Initio Study of a Cubic Perovskite: Structural, Electronic, Optical and Electrical Properties of Native, Lanthanum- and Antimony-Doped Barium Tin Oxide. *Material Science in Semiconductor Processing*, **32**, 100-105. <https://doi.org/10.1016/j.mssp.2014.12.031>
- [57] Mott, N.F. (1990) Metal Insulator Transitions. Taylor and Francis, London.
- [58] Ravi, S. and Kar, M. (2004) Study of Magneto-Resistivity in La<sub>1-x</sub>Ag<sub>x</sub>MnO<sub>3</sub> Compounds. *Physica B*, **348**, 169-176. <https://doi.org/10.1016/j.physb.2003.11.087>
- [59] Sarma, D.D., Chainani, A., Krishnakumar, S.R., Vescovo, E., Carbone, C., Eberhardt, W., Rader, O., Jung, C., Hellwig, C., Gudat, W., Srikanth, H. and Raychaudhuri, A.K. (1998) Disorder Effects in Electronic Structure of Substituted Transition Metal Compounds. *Physical Review Letters*, **80**, 4004-4007. <https://doi.org/10.1103/PhysRevLett.80.4004>
- [60] Jung, W.H. (1998) Evaluation of Mott's Parameters for Hopping Conduction in La<sub>0.67</sub>Ca<sub>0.33</sub>MnO<sub>3</sub> above T<sub>c</sub>. *Journal of Materials Science Letters*, **17**, 1317-1319. <https://doi.org/10.1023/A:1006665200481>
- [61] Mott, N.F. and Davis, E.A. (1971) In Electronics Process in Non-Crystalline Materials. Clarendon, Oxford.
- [62] Viret, M., Ranno, L. and Coey, J.M.D. (1997) Magnetic Localization in Mixed-Valence Manganites. *Physical Review B*, **55**, 8067-8070. <https://doi.org/10.1103/PhysRevB.55.8067>
- [63] Millis, A.J., Littlewood, P.B. and Shraiman, B.I. (1995) Double Exchange Alone Does Not Explain the Resistivity of La<sub>1-x</sub>Sr<sub>x</sub>MnO<sub>3</sub>. *Physical Review Letters*, **74**, 5144-5147. <https://doi.org/10.1103/PhysRevLett.74.5144>
- [64] Jonscher, A.K. (1977) The "Universal" Dielectric Response, *Nature*, **267**, 673-679. <https://doi.org/10.1038/267673a0>
- [65] Hirose, N. and West, A.R. (1996) Impedance Spectroscopy of Undoped BaTiO<sub>3</sub> Ceramics. *Journal of the American Ceramic Society*, **79**, 1633-1641. <https://doi.org/10.1111/j.1151-2916.1996.tb08775.x>